Improved Bi-Criterion Flexible Registration for Fixtureless Inspection of Compliant Parts

Kaveh Babanezhad, Ali Aidibe, Gilles Foucault, Antoine Tahan, Jean Bigeon

Improved Bi-Criterion Flexible Registration for Fixtureless Inspection of Compliant Parts

Kaveh Babanezhad[a], Ali Aidibe[b], Gilles Foucault[a,*], Antoine Tahan[b], Jean Bigeon[a]

[a]Univ. Grenoble Alpes, CNRS, Grenoble INP, G-SCOP, F-38000 Grenoble, France
[b]École de technologie supérieure, 1100 Notre-Dame St. West, Montreal H3C 1K3, Canada
** Corresponding Author*

kaveh.babanezhad@univ-grenoble-alpes.fr

ali.aidibe.1@etsmtl.net

gilles.foucault@univ-grenoble-alpes.fr

antoine.tahan@etsmtl.ca

jean.bigeon@grenoble-inp.fr

Abstract

Because of the effects of gravity and/or residual stress, some manufactured mechanical parts, such as sheet metals and skins, often have a significantly different shape in a free-state position as compared to their state-of-use position. These parts are described as compliant, flexible or nonrigid. Expensive specialized fixtures are currently used prior to performing geometrical inspection operations in order to maintain compliant parts in the state-of-use position. This paper introduces an automatic bi-criterion flexible registration method for the dimensional and geometric inspection of such parts. The proposed method deforms the data acquired via a non-contact scanner of a compliant part in a free-state position until it reaches the nominal CAD shape for inspection with conventional Computer-Aided Inspection (CAI) tools. In other words, the method neutralizes the deviations induced in a compliant part by the effects of gravity and residual stress, allowing the acquired data to be treated as if it were obtained from a rigid part, using already available conventional (rigid) CAI tools. A proposed algorithm based on the BOFR-2 (the **2**nd version of a **B**i-**O**bjective **F**lexible **R**egistration algorithm) method is validated against both virtual simulated and experimental real industrial case studies from the aerospace sector. The resulting cost reduction and agility increasing make this fixtureless method well adapted to the requirements of unit-batch production in the context of Industry 4.0.

Keywords: Metrology ; Fixture ; Inspection ; Nonrigid ; Flexible ; Compliant

1 Introduction

In manufacturing, quality control (QC) is an essential phase as it guarantees that customers will receive parts within a permissible tolerance. Given that all manufactured parts often have geometrical differences versus their nominal Computer-Aided Design (CAD) models, performing an inspection becomes critical during the QC phase. For rigid parts, this inspection is typically performed in two steps. First, there is preliminary geometric data acquisition in the state-of-use (~ assembly) position (contact-based or non-contact acquisition). Acquired data are usually exported in a standard PointCloud file format or in a triangular surface mesh file format (e.g., *.STL). Second, processing is performed to acquire data using 3D optical scanner and Computer-Aided Inspection (CAI) tools to identify the location and amplitude of manufacturing defects (depending on predefined tolerance types and tolerance ranges). This two-fold inspection routine is currently limited to only parts that are reasonably rigid. This focus on rigidity is due to conventional CAI software requirements, in which it is assumed by default that any data imported into the software is from a rigid part, and thus, any deviation (outside typical measurement equipment noise amplitudes) between the imported data and the nominal CAD model should be treated as a potential manufacturing defect. Some mechanical parts, such as parts with thin walls (skins), have a considerably different shape in a free-state condition as compared to their nominal CAD model due to the effects of gravity and residual stress remaining from manufacturing processes. This geometric deviation results mostly from such elastic deformations, rather than from actual manufacturing defects. The notion of flexibility of *compliant* parts was first quantified in [3] (they are also sometimes called *nonrigid*, *flexible parts* or *deformable bodies*). The geometrical inspection of compliant parts requires an extra step because of the aforementioned geometric deviation they entail, over and above the standard quality control of rigid parts. Traditionally, standard or specialized conformation fixtures must first be set up to maintain the part in its state-of-use position as defined in a CAD model.

There are multiple downsides to using fixtures, including the time-consuming set-up process, considerable purchase and operating expenses, and errors in CAI analysis if the setup on the fixture has not been performed adequately. These disadvantages have recently led researchers to attempt to circumvent the use of fixtures with **flexible registration with complementary defect identification** [1]–[18]. A flexible registration is a deformation of the acquired point set that respects intrinsic (dimensional and shape) properties of the compliant part in order to avoid the misidentification of any existing defects or create new artificial ones. The flexible point set registration could be based on a Finite Element Analysis (FEA) [4], [14] or on a probability density estimation [15], [16]. FEA-based flexible registration methods have major disadvantages, such as being difficult to set up (e.g., properly defining boundary conditions) and require significant computational resources. Probabilistic flexible registration methods have managed to increase automation and reduce runtimes. However, these methods have not been extensively explored in previous research, and are still in their early-to-intermediate stages of maturity. In 2011, the Iterative Displacement Inspection (IDI) algorithm [19] was introduced. This essentially initiates the Nonrigid-ICP [20] registration algorithm iteratively to register CAD meshes onto SCAN meshes, while minimizing two objective functions: the point-to-point distance between SCAN and CAD and a scalar representation of the change in the smoothness of the CAD mesh per (registration) iteration. Minimizing the change in smoothness was meant to ensure (by association) the integrity of the intrinsic (dimensional and shape) properties of the part during registration. In 2015, a method and an algorithm based on it, named Inspection of Deformable Bodies by Adapting the Coherent Point Drift (IDB-ACPD), was introduced [15]. The Coherent Point Drift (CPD) [21] nonrigid registration is initiated iteratively to register CAD meshes onto SCAN meshes, while minimizing two objective functions: the point-to-point distance between CAD and SCAN and a scalar representation of the change in mesh size parameter (or stretch) of the CAD mesh per iteration. The minimization of the change in mesh size parameter was meant to ensure the integrity of the intrinsic properties of the part during registration. In summary, both IDI and IDB-ACPD propose a CAD-to-SCAN registration

direction (similar to the finite-element-based methods that followed after [5], [6], constraining the registration in one way or another to ensure integrity of the part during registration, a pointwise distance calculation between CAD and SCAN, and a single-objective formulation for finding the ideal registration parameters. Haj Ibrahim et al. in [22] extended ACPD registration method to sheet-metal parts featuring rigidity variations located in high-curvature regions. They incorporated a weight matrix to adjust the stretch conservation criterion at each measurement point, and therefore simulate the part rigidity locally during the ACPD registration operation. A surface segmentation classifies zones featuring similar curvature and rigidity. The local weight affected to each zones is a new parameter of the registration loop.

Alternative **standalone defect identification** methods do not necessarily rely on a prior flexible registration operation (although it could possibly benefit from one as a bonus). Despite recent developments and its theoretical superiority to complementary methods, standalone defect identification is still very new, and lacks the accuracy of a complementary defect identification performed after a flexible registration [3], [13].

Another research trend is assembly Assessment methods to predict the behavior of compliant parts in an assembly, such as the optimal assembly sequence and its effects on the final shape [17], the post-assembly shape of a compliant part under normal lighting conditions [18], and the required assembly boundary conditions to ensure a post-assembly shape that closely resembles the nominal CAD [23], [24]. They are typically performed after the conclusion of complementary defect identification (they thus rely on a prior near-perfect flexible registration performed outside, or as part of their own proposed method). [25] proposed an extension of the Statistical Variation Analysis and FEA (SVA-FEA) methodology. Two consecutive FEA are run: first, a linear model of flexible assembly analysis is used to calculate the forces needed to fixture and fasten parts in all points of interest. Second, opposite forces are applied to simulate the elastic spring-back effect occurring during the releasing phase of fixture and fasten tools. In order to avoid part-to-part penetration in the fastening and during spring-backphase, multi-point contact constraints are introduced. Franciosa et al. proposed in [26] a systematic methodology to optimize the fixture layout design, by efficiently determining the manufacturing variability in function of the location and number of clamps and locators, in presence of stochastic manufacturing errors both at product and process levels. Gouyou et al. [27] used the polytope form tolerance simulation and local contact finite element analysis to identify compliant part's deformations induced by the assembly. The pressure resulting from contact zones is used to evaluate the difficulty level of the assembly.

In this paper, an additional installment to the probabilistic flexible registration category is proposed, which minimizes non-flexible deformations, and validates the deformation locally with a rigorous metric. The method is named BOFR-2 (2^{nd} version of a Bi-Objective Flexible Registration algorithm), with the first version having been briefly presented in [1]. The proposed methodology is validated by tests against multiple virtual (simulated) and experimental (real) industrial case studies. The contributions of the proposed method to the state of the art include improvements in terms of accuracy, automation, runtime, robustness and precision (repeatability), and interoperability.

The paper is organized as follows: The proposed method is presented in Section 2. The validation approach is explained in Section 3.1, while the results obtained are presented in Sections 3.2 and 3.3. A discussion of the interpretation of the results is carried out in Section 4, and concluding remarks and future works are presented in Section 5.

2 Methodology

In this work, defects were analyzed in accordance with ISO-1101:2017 Geometrical Product Specifications (GPS) standards [28]. The underlying concept behind the method can be simplified as follows: a bi-objective optimization is performed to minimize two key criteria that are the output of a

black box containing a nonrigid registration algorithm. The input is a selection of parameters of the nonrigid registration algorithm chosen to be inside the black box. The nonrigid registration algorithm will register a previously defined source point cloud onto a target point cloud (each time the black box is initiated). The first output of the black box is a Hausdorff distance criterion between the registered source point cloud and the target point cloud. The second output is a criterion quantifying the change in dimensional and shape properties of the source point cloud. The main steps of the method developed are presented in Algorithm 1. All computational operations in this study were performed on a dual-core Intel Core® i5-4300U machine clocked at 1.9 GHz and equipped with 4.0 GB of RAM and the 64-bit MS Windows® operating system. BOFR-1/2 were developed in MATLAB® (R2016a) as single-threaded applications.

Algorithm 1 – Main steps of the proposed (BOFR-2) method

Inputs: CAD mesh, SCAN mesh, mesh size *T*, CPD smoothness regularization parameters lambda=lambda_init and beta=beta_init; noise/outliers handling parameter ω
Outputs: OPTREG optimally registered mesh, and defects.
Repeat:

1. Register SCAN mesh to CAD mesh using the flexible registration algorithm (CPD), save it as REG mesh
2. Compute the Hausdorff Distance between REG and CAD meshes defined as the largest distance between REG vertices and CAD triangles
3. Compute the strain criterion defined as the norm of δ_{STi}: the largest deformation from SCAN to REG of j edges $E_{i,j}$ adjacent to vertex V_i.
4. Optimize lambda and beta parameters with both strain and distance objectives,

Until a stopping criterion is reached, i.e., maximum number of overall (black box) function evaluations, and maximum number of iterations.

5. Compute the distance/strain Pareto front with optimal candidates (lambda_opt, beta_opt), and save OPTREG, the optimal solution using the optimality heuristic "quality of the superposition"
6. Manual defects identification on OPTREG
7. Automatic defects identification on OPTREG

2.1 Step #1 and Step #4 (Optimizer and Registrar)

Theoretically, any branch of nonrigid registration algorithms capable of performing a free-form alike deformation can be used. Various nonrigid registration methods are surveyed in[29], with the CPD algorithm chosen to be used [21]. This choice was thanks to its good ability to register large point clouds, an internal noise handling ability, its proven usability in the context of flexible registration, and its proven superiority over other nonrigid registration methods such as [30]–[33].

The CPD smoothness regularization registration parameters are λ and β, and the noise/outliers handling parameter is ω (enabling implicit noise handling in BOFR). It is worth mentioning that in CPD, input parameter β defines the model of the smoothness regulator (i.e., it controls the rigidity and locality of the spatial smoothness), and parameter λ defines the tradeoff between the goodness of the maximum likelihood fit and regularization (i.e., it sets the strength of β). The overall approach of CPD in the nonrigid registration of point clouds can be simplified as follows. The superposition of two (source and target) point clouds is considered as a probability density estimation, where the source point cloud represents a set of Gaussian Mixture Model (GMM) centroids and the target point cloud represents a set of data points onto which the GMM centroids would be fitted. The fitting of GMM centroids is then performed iteratively via an Expectation Maximization (EM) optimization [34], [35] by calculating the posterior probabilities of the centroids' fit. This maximization intends to find the best correspondence probability between the points of the two point clouds. A constraint is also considered during the maximization: forcing the GMM centroids to move coherently as a group (as defined by the

Motion Coherence Theory (MCT) in [36] in order to minimize the deformation of the source point cloud. The BOFR performs the registration in the SCAN-to-CAD direction. This increases the interoperability of the BOFR results since the free-state SCAN meshes registered by the BOFR can then be directly used to perform not only a complementary defect identification, but also an assembly assessment.

As for the optimization of objectives (Step #4 in Algorithm 1), in the BOFR, a bi-objective optimization approach was adopted. This optimization is often used where the optimal solution to a problem needs to be reached in the presence of two conflicting objectives. Such problems often lack a solution that simultaneously optimizes both objectives, and a possible infinite number of solutions can be found. In engineering terminology, a solution is called non-dominated (or Pareto optimal) if none of the objective functions can be improved in value without degrading other objective function values. The Pareto front is then defined as the set of choices that are Pareto optimal, and in the case of two objectives, depicted as a two-dimensional (tradeoff) curve. By restricting attention to the Pareto front members, a decision maker could make tradeoffs within a small non-dominated set, rather than consider the full range of every parameter. In the BOFR, we are minimizing a distance criterion and a criterion quantifying the change in the intrinsic dimensional and shape properties of the source point cloud. The conflict can be summarized as follows: we want the distance between the source and target point clouds after registration to be as close as possible to zero, but that is only achievable with high values for the second criterion (yet we also do not want to let that happen and obtain near-zero values for the second criterion as well). Thus, the task at hand becomes a black box optimization problem with two objectives as outputs. Typical characteristics of black box optimization include the lack of any prior knowledge of the problem and the need for the black box to have a nonlinear behavior. These characteristics fit our context as the CPD registration cannot be estimated a priori because it lacks derivative information and prior Pareto front shape. Figure 1 shows the behavior of the CPD procedure (the objective Black-Box function). As a result, a particular branch of black box optimization methods needs to be used. Such methods have been extensively surveyed in [37], and include the Mesh Adaptive Direct Search (MADS) algorithm [38], [39] in its bi-objective format. The BiMADS algorithm [38] has been chosen for two reasons. Firstly, the behavior of BiMADS is deterministic, as it approximates the same Pareto front regardless of how many times it has been initiated from the same initial guess. Secondly, its convergence and its optimality are mathematically proven.

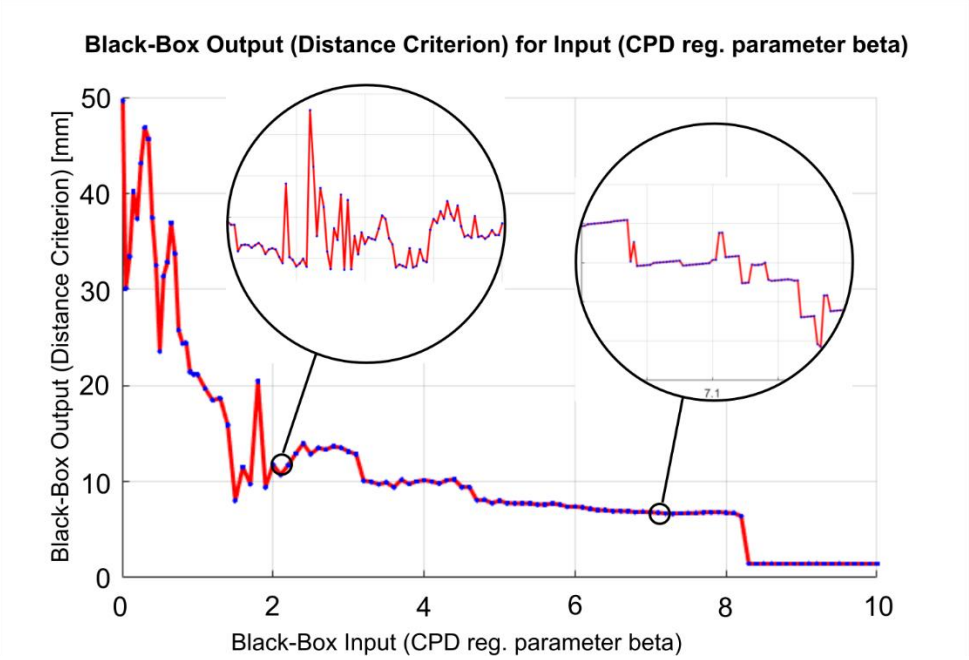

Figure 1 –Behavior of BOFR-1/2 Black-Box function

2.2 Step #2 (Distance Criterion)

The first of the two outputs of the black box to be minimized, referred to as the distance criterion, calculates the Hausdorff distance between the source and the target triangular meshes (named REG and CAD) after each registration process in the optimization loop. Let $RV = \{v_{r1}, v_{r2}, \dots, v_{rn} | v_{ri} \in \mathbb{R}^3\}$ be the set of n vertices extracted from the source mesh file (REG); $CV = \{v_{c1}, v_{c2}, \dots, v_{cn'} | v_{ci} \in \mathbb{R}^3\}$ the set of n' vertices extracted from the target mesh file (CAD); $RT = \{t_{r1}, t_{r2}, \dots, t_{rm} | t_{rj} \in \mathbb{R}^{3x3}\}$ the set of m triangles belonging to the source mesh file (REG), where each t_{ri}contains vertices' coordinates of the *i-th* triangle, and similarly let $CT = \{t_{c1}, t_{c2}, \dots, t_{cm'} | t_{cj} \in \mathbb{R}^{3x3}\}$ be the set of m' triangles belonging to the target mesh file (CAD). A *directed* source-to-target mesh Hausdorff distance ($h(RV, CT)$) could then be described as the *"maximum vertex-to-triangle distance of the set RV to the nearest triangle in the set CT"*. In mathematical form, it can be written as in Eq.1:

$$h(RV, CT) = \max_{v_{ri} \in RV} \{ \min_{t_{cj} \in CT} dist(v_{ri}, t_{cj}) \} \qquad \text{Eq. 1}$$

where $dist$ is a function programmed to calculate the distance between a vertex and a triangle. Similarly, a directed target-to-source Hausdorff distance can be calculated and denoted by $h(CV, RT)$. The *two-way* or *cumulative* Hausdorff distance would be defined in Eq.2:

$$H_d(RV, CT) = \max \{ h(RV, CT), h(CV, RT) \} \qquad \text{Eq. 2}$$

where H_d is the distance criterion used as one of the cost functions in the optimization loop. For an absolutely perfect superimposition, this value would be equal to zero.

2.3 Step #3 (Stretch / Strain Criterion)

The second output of the black box to be minimized can be set to either calculate the same stretch criterion of [15] or to use an alternative referred to in this chapter as the strain criterion. In the BOFR, the stretch criterion provides a cumulative measure of the change in the average of geodesic distances

(equal to mesh sizes) between each vertex and its neighbors on the same mesh after the mesh has been registered to a new shape during the optimization process. Let RV and RT be the same sets defined in the description of the distance criterion (step #2). The stretch differences δ_{SC} and stretch criterion Δ_{SC} are then respectively defined in Eq.3 and in Eq.4:

$$\delta_{SC} = N^{-1}\left|\sum_{i=1}^{N} D_{R,i} - \sum_{i=1}^{N} D_{S,i}\right| \quad \text{Eq. 3}$$

$$\Delta_{SC} = \sqrt{\frac{\sum\|\delta_{SC}\|^2}{n-1}} \quad \text{Eq. 4}$$

where N is the number of neighbors around vertex v_{ri}; $D_{R,i}$ is the average distance between v_{ri} and its neighbors, and Δ_S is the Euclidean norm of differences in δ_S between the initial (SCAN) and the registered (REG) mesh. A low value of the stretch means that the registration conserves the distances between nodes and their neighbors. In this paper, the new strain criterion provides a cumulative measure of the biggest rate of change in the edge mesh sizes linking each vertex to its neighbors after the mesh has been registered to a new shape during the optimization process. Let RV and RT be the same sets defined in the description of the distance criterion (step #2). The strain differences δ_{ST} (column vector of size $n \times 1$) and the strain criterion Δ_{ST} (scalar value) are then respectively defined in Eq.5 and Eq.6:

$$\delta_{STi} = \max\left(\frac{\left|D_{R,i} - D_{S,i}\right|}{D_{S,i}}\right) \quad \text{Eq. 5}$$

$$\Delta_{ST} = \sqrt{\frac{\sum\|\delta_{ST}\|^2}{n-1}} \quad \text{Eq. 6}$$

where n is the number of vertices in RV; $D_{R,i}$ is a matrix whose *i-th* row contains all the distances between v_{ri} and its immediate neighbors, and Δ_{ST} is the Euclidean norm of differences in δ_{ST} between the initial (SCAN) and the registered (REG) mesh. In other words, the column vector δ_{ST} represents the per-vertex maximum engineering strain for all vertices of the registered (REG) mesh, and Δ_{ST} is the Euclidean norm of differences in the set of per-vertex maximum strains. Furthermore, a correlation can be assumed between the per-vertex maximum strain (δ_{ST}) and an overall strain (typically denoted by ε) that respects the Von Mises yield criterion. Under that assumption, because the material properties of a part, such as the tensile yield strength and the Young's modulus, are known, a hard limit on the overall strain (ε), and by association δ_{ST}, could be calculated to ensure that the registration respects the Von Mises yield criterion [24]. Such a registration is guaranteed to not create new defects in the acquisition data while registering it. The aforementioned hard limit can be programmed either as a constraint for the optimization problem to be solved by BiMADS, or as an additional cost function to be minimized. Finally, Figure 2 illustrates the superiority of the new strain criterion of BOFR-2 over the stretch criterion used in the BOFR-1.

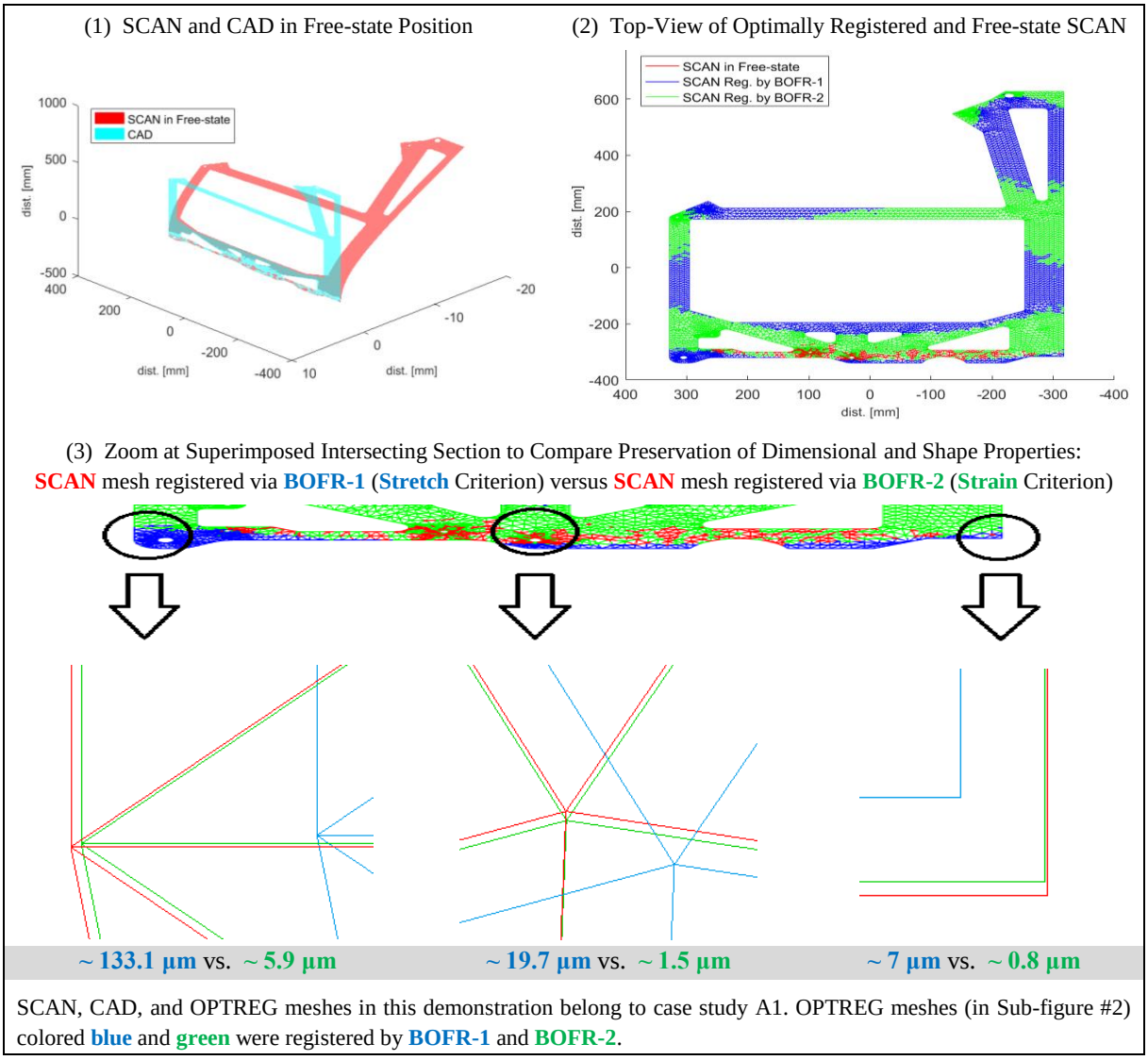

Figure 2 – Comparison of the effects of stretch and strain criteria in preserving dimensional and shape properties

2.4 Step #5 (Optimality Heuristics)

The role of the optimality heuristics is to help determine the member of the resulting two-dimensional Pareto front that is the best pick, which removes the need for end-user involvement. In the BOFR-2, the two elements of the cost function are the scalar distance and the strain values. To improve the decision-making process, a third dimension is subsequently inserted into this set. Here, each third dimension describes the quality of the superposition obtainable by that front member. For an obtained 2D Pareto front with k members, this quality of superposition, which is termed QoS, is defined in Eq.7:

$$QoS = \{ q_1, \dots, q_k | q_l = 100 - \%\left(\min_{t_{cj} \in CT} dist(v_{ri}, t_{cj}) < 0.025\ mm \right) \} \qquad \text{Eq. 7}$$

where v_{ri}, t_{cj} and $dist$ are the same as described in sub-sections 3.2 and 3.3. Each RV_l is a set composed of registered vertices that resulted in the *l-th*-obtained 2D Pareto front member. A small QoS value for a 2D Pareto front member indicates that the registration associated with that member resulted in a good superposition between the source (SCAN) and target (CAD). The 25 µm distance in Eq. represents the value of the measurement equipment noise : a handheld optical 3D scanner "MetraScan" from Creaform. The QoS is calculated for each member of the initial 2D Pareto front and extends the N 2D-

points of the Pareto front to a vector of N 3D-points: $\overrightarrow{P_l}$=($H_d(RV_l, CT)$, $\Delta_{ST}(RV_l)$, $QoS(RV_l)$), where $l \in [1; N]$. The point $\overrightarrow{P_l}$ having the shortest distance to the origin is chosen as the best solution.

2.5 Steps #6 and #7 (Defect Identification)

As mentioned earlier, given a satisfactory flexible registration (i.e., the majority of the source mesh vertices are correctly superimposed on the target mesh vertices), the registered scan (OPTREG in Algorithm 1) can then be treated as a rigid part's scan inside conventional CAI software (e.g., Polyworks®). In this study, two types of defects are considered: contour profile defects and hole center localization defects, between OPTREG and CAD.

2.6 Steps #8 and #9 (Mesh Generation and Mesh Simplification)

As presented in Algorithm 1, a surface mesh is generated on the nominal CAD. In this study, the Delaunay triangulation provided via the mesh generator within SolidWorks® Simulation Standard was used to create a surface mesh on the nominal CAD [40]. The created mesh is dubbed 'standard' in the software (as opposed to a curvature-based mesh). Mesh edge lengths automatically proposed by the software (which typically amount to an efficient number of vertices to accurately represent the part's geometry) were used in the mesh generation operation.

It is proposed that the acquisition data (SCAN) undergo a mesh simplification operation. This is applied only to the experimental case studies in order to avoid using over-sampled raw acquisition data, since it would severely affect algorithm runtimes without providing any positive gain in the accuracy of the final results. The mesh was simplified using the quadratic edge collapse decimation from MeshLab [41]. In terms of the adopted configuration, a threshold on the maximum number of triangles was manually set for each experimental case study (E1 and E2). Information regarding the chosen thresholds and the resulting SCAN meshes (E1 and E2) are gathered in Table 1. Furthermore, the CAD meshes in the experimental case studies were also simplified since they were created differently from the virtual case studies. A lower threshold for the mesh simplification of the CAD meshes was chosen in order to adhere to the initial assumptions of the study. The compliant virtual case studies parts were simulated by SolidWorks Simulation® (finite element analysis) to identify gravity deformations. Starting with the CAD model, the scanned manufactured part (with defects) was simulated in accordance. Predefined profile deviation (defect) was added to all virtual case studies (See section 3.1.1, Table 2 to Table 4).

Table 1 – Mesh Information of Case Studies

Case Study		# of Vertices	# of Edges	# of Triangles	Density [vertices per cm^2]
A1	SCAN	4010	10976	6952	2.40
	CAD	1131	2886	1741	0.67
A2	SCAN	4010	10976	6952	2.40
	CAD	1131	2886	1741	0.67
A3	SCAN	4010	10976	6952	2.40
	CAD	1131	2886	1741	0.67
B	SCAN	4019	10989	6956	2.46
	CAD	1130	2877	1733	0.69
C	SCAN	3858	10673	6796	0.55
	CAD	1069	2785	1697	0.15
D	SCAN	11053	32219	21156	1.19
	CAD	2882	8187	5295	0.31
E1	SCAN	6613	16620	**9999**	5.34
	CAD	4112	9120	**5000**	3.32
E2	SCAN	6468	16474	**9999**	4.92
	CAD	3932	8939	**5000**	2.98

* A1 to D are virtual (simulated) case studies; E1 and E2 are experimental (real) case studies

2.7 Step #10 (Display of Identified Defects)

This step involves the mechanism required to display and clarify the location of any existing manufacturing defects. The amplitude for any potential manufacturing defect has already been calculated in step #7 via a set of distance-based tools programmed to mimic the behavior of the previously described manual tools of step #6. In step #10, using the assigned amplitudes, the intent is to clarify which of the vertices are in a defect region. This can be done either via an interaction with the end-user, or automatically. Traditionally, a color map displays the calculated amplitude for each vertex of the acquisition data. Such an amplitude could be the distance difference between each vertex of the registered SCAN mesh and its corresponding vertex on the nominal CAD mesh. Alternatively, outlier detection methods such as the maximum normed residual test (also known as the Grubbs' test) could be applied to a set composed of the amplitudes for all vertices.

3 Results

3.1 Validation Approach and Assumptions

In order to investigate the claims of the proposed methodology, the BOFR-2 (alongside its initial version, BOFR-1) was tested against both virtually created case studies (mostly from the aerospace industry) and experimental (real) ones. The following assumptions were initially made in this study:

(1) The part material is known (Aluminum 7050), and the CAD model is available. Moreover, the triangulated point cloud (mesh) of the scanned part available is not a partial scan, and has reasonably clean boundaries (imperfections at worst below 10% of the part's overall profile tolerance range). The geometric deviation at the free-state position must also be above the overall profile tolerance range.

(2) The mesh density of the scanned part is higher than the mesh that will be generated on its corresponding CAD (at least two to three times higher). A low density (coarse) mesh of a part in the free-state position might not represent all the actual details (potential defects) due to the considerable gravity-induced deformation that exists in the free-state position. The same resolution is not needed on the nominal CAD mesh, given that flat regions are known (there is no defect on the CAD) and can be represented accurately even with a lower density mesh.

(3) Data acquisition equipment noise is much smaller than defect amplitudes. Defect areas do not cover the majority of the part. Inspection is in accordance with the standard definition (e.g., ISO-GPS standards). In this paper, inspection is limited to localization defects and contour profile errors.

3.1.1. Case Studies

A virtual (simulated) case study was comprised of the CAD model of an industrial part, which was then modified to contain a number of artificial defects (contour profile errors and hole center localization), and was subsequently deformed under simulated gravity in a finite element software application, resulting in a virtual SCAN in the free-state position. The deformed finite element surface mesh was exported (OFF file format), acting as a virtual SCAN of the part in its free-state condition. In terms of software resources, SolidWorks® was used for the finite element operations. This was followed by a meshing operation on the CAD, and the resulting surface mesh being exported in OFF file format. Finally, a simulated Gaussian measurement equipment noise was added to the OFF mesh of the virtual SCAN. An experimental (real) case study is comprised of a CAD model of a real part, and real SCAN data captured from it via a non-contact acquisition hardware.

3.1.2. Evaluation Metrics

The overall performance is evaluated by comparing the estimated defect amplitudes at specific regions with the predefined known defect amplitudes of the (virtual and experimental) case studies.

Two metrics can be considered in describing the error in estimating the defect amplitudes via an algorithm. The first, a relative Metrological Algorithmic Error (MAE), is defined in Eq.8:

$$MAE = \frac{v_{abs}(KDA-EDA)}{Tol} \qquad \text{Eq. 8}$$

where $v_{abs}(x)$ is the function returning the vector of absolute values of a vector x, KDA is a vector representing *known* vertex defect amplitudes, EDA is a vector representing the *estimated* vertex defect amplitudes, and Tol is the overall tolerance range for the part. The following categorization for the MAE values could be used:

$$\begin{aligned} MAE &< 10\% && \text{highly desirable} \\ 10\% < MAE &< 30\% && \text{acceptable} \\ MAE &> 30\% && \text{unusable} \end{aligned}$$

In other words, as long as the MAE associated with an algorithm is < 30%, its obtained results (estimated defect amplitudes) can replace the traditional fixture-based inspection results. The second error metric, a Statistical Algorithmic Error (SAE) is defined in Eq.9:

$$SAE = q_{95\%}\,(\,|\,KDA - EDA\,|\,) \qquad \text{Eq. 9}$$

where $q_{95\%}$ is the 95th percentile of the vector of absolute differences between known defect amplitudes and estimated defect amplitudes. SAE is a scalar (e.g., in μm or mm) describing a type of worst-case scenario in which in 95% of cases, the error is below or at the aforementioned scalar value. In other words, the SAE is a kind of worst limit statistical metric that is not linked to the tolerance ranges of the part, and any algorithm that has a lower SAE value (compared to others) is performing better.

A final evaluation was also conducted by applying the BOFR-1/2 on two experimental case studies. Validations against experimental case studies demonstrate the algorithm's ability to work with real acquisition data.

3.2 Virtual Case Studies

The majority of the mechanical parts used in virtual case studies come from the aerospace industry, where profile tolerance ranges are typically between 0.8 to 1.6 mm (in our case, 1 mm was considered). The measurement equipment noise added to the virtual scan was chosen to 25 μm (at 95% confidence level). A top view of each of the virtual case studies (known defect regions in red) is depicted in Figure 3. Some of the defects have an amplitude of zero microns, and were defined as such in the virtual scans to quantify possible over-estimations of defect amplitudes, and whether there is a correlation between estimated and actual defect amplitudes. The actual known amplitudes of these induced defects are available in tables positioned to the right of Figure 3.

An example of results processed via the semi-automated procedure when validating the BOFR against the virtual case studies is presented in Figure 4. Figure 4.1 depicts the SCAN in its free-state position. Figure 4.2 depicts the known defect regions and their amplitudes. Figure 4.3 shows the cumulative distribution function (CDF) of all per-vertex metrological algorithmic errors for known defects. Figure 4.4 to Figure 4.7 present the color map for both algorithms (BOFR-1 and BOFR-2) of the estimated surface profile deviations and the estimated per-vertex defect amplitudes for known defect regions, respectively. Figure 4.8 and 4.9 present the per-vertex strains on the registered SCAN, as compared to its state before registration. Typically, with the strain criterion, the BOFR-2 tends to have lower per-vertex strain values.

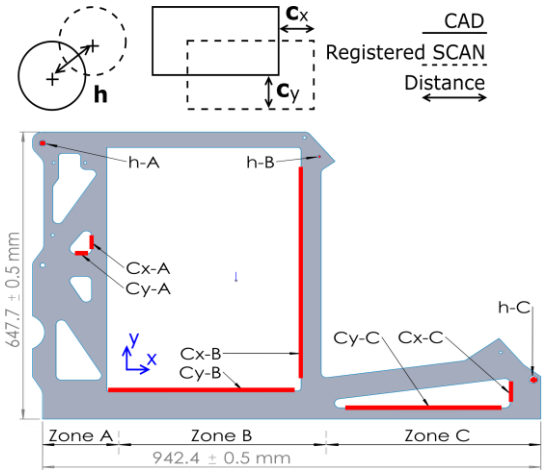

Case B

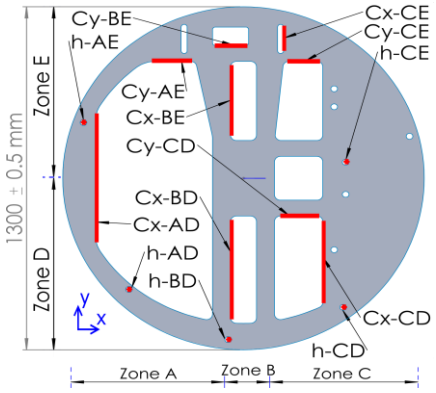

Case C

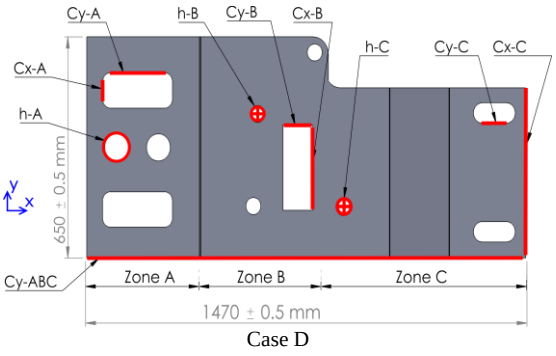

Case D

Table 2 – Case B, Defect amplitude estimations (manual measurement)

Defects (**in µm**)		Zone A	Zone B	Zone C
Hole (**h**)	Actual	**300**	**800**	**0**
	BOFR1	204	813	21
	BOFR2	**221**	**803**	**18**
Contour (**c_x / c_y**)	Actual	**0 / 800**	**300 / 0**	**800 / 300**
	BOFR1	**23** / **778**	213 / 8	776 / **277**
	BOFR2	24 / 776	**216** / **6**	**789** / 273

Table 3 – Case C, Defect amplitude estimations (manual measurement)

Defects (**in µm**)		Zone AD	Zone AE	Zone BD	Zone BE	Zone CD	Zone CE
Hole (**h**)	Actual	**300**	**800**	**0**	**-**	**1500**	**1000**
	BOFR1	**164**	848	**9**	-	**1503**	**786**
	BOFR2	160	**844**	**9**	-	**1503**	785
Contour (**c_x / c_y**)	Actual	**800 / -**	**- / 0**	**300 / -**	**0 / 800**	**1500 / 300**	**300 / 800**
	BOFR1	**726** / -	- / 6	223 / -	19 / 15	**1454** / 305	**263** / **790**
	BOFR2	719 / -	- / **5**	**224** / -	**17** / **13**	1452 / **304**	262 / **790**

Table 4 – Case D, Defect amplitude estimations (manual measurement)

Defects (**in µm**)		Zone A	Zone B	Zone C	Zone ABC
Hole (**h**)	Actual	**300**	**0**	**800**	**-**
	BOFR1	**303**	34	651	-
	BOFR2	347	**28**	**710**	-
Contour (**c_x / c_y**)	Actual	**800 / 300**	**300 / 800**	**0 / 300**	**- / 0**
	BOFR1	**746** / **309**	202 / 677	29 / 242	- / 54
	BOFR2	695 / 335	**204** / **751**	**28** / **297**	- / **52**

Figure 3 – (a) Defects and analyzed dimensions, (b) Top-view of the B/C/D case studies (best estimations are underlined and in bold)

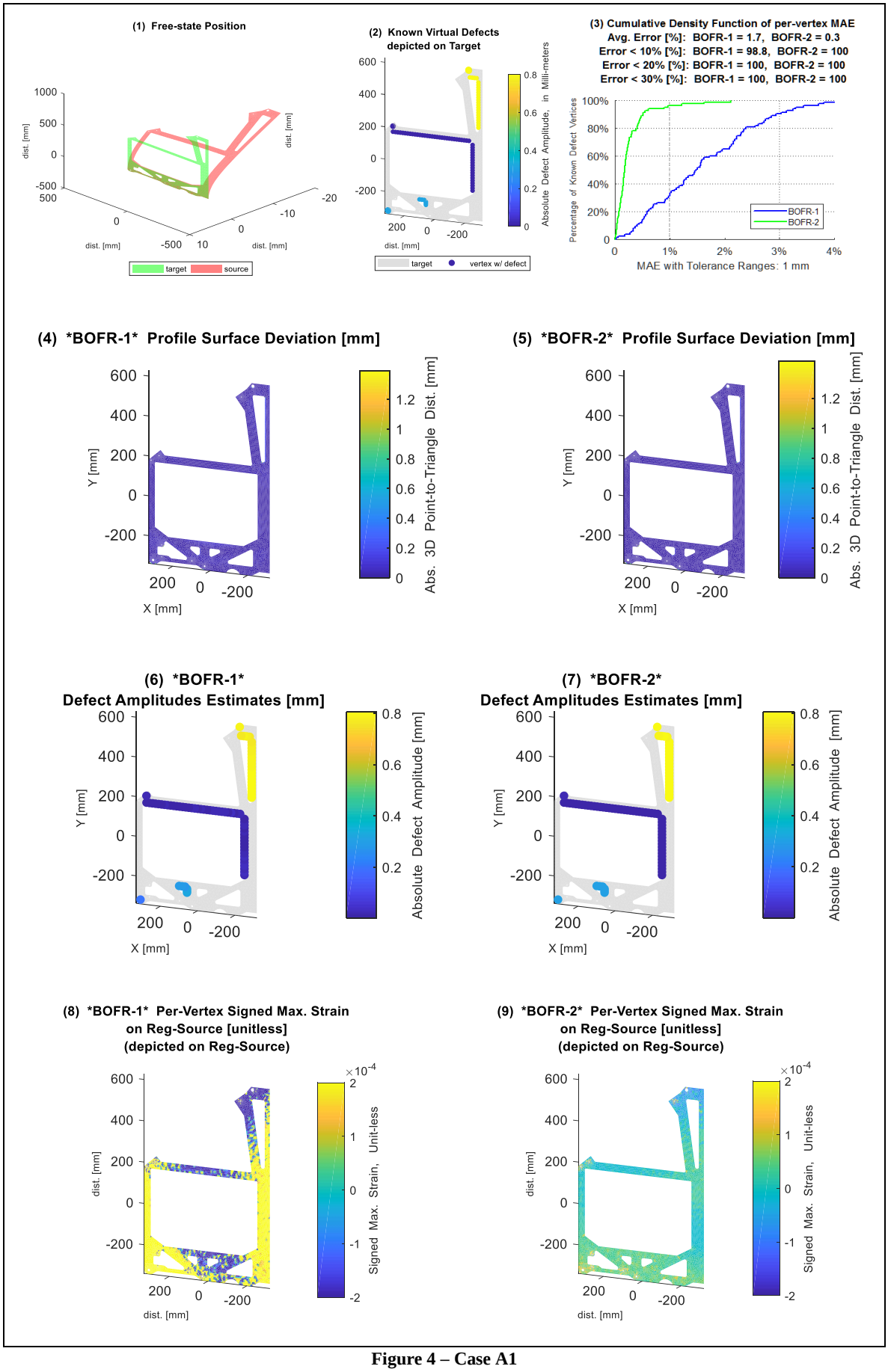

Figure 4 – Case A1

3.3 Experimental Case Study

Data acquisition was performed from real parts using a laser scanner (Creaform® MetraScan). Conformation fixtures were not used, and parts were merely placed on a simple support to distinguish the surface of the part during scanning from the background scenery. The overall tolerance range for the experimental case studies was set to 2 mm. This choice is justified by the larger amplitude of known defects of this experimental case and by the handled scanner accuracy. The experimental case studies (E1 and E2) consisted of two quasi-planar aluminum parts containing multiple small structured grooves (originally manufactured for a former study [42], with differences in both their CAD definitions and their deformed shape in free-state position). Cases E1 and E2 are depicted in Figure 5 in their respective free-state shapes, with a top view of each one. Table 5 and Table 6 also contain the post-registration manually measured defect amplitudes. The results processed are shown in Figure 6 and Figure 7.

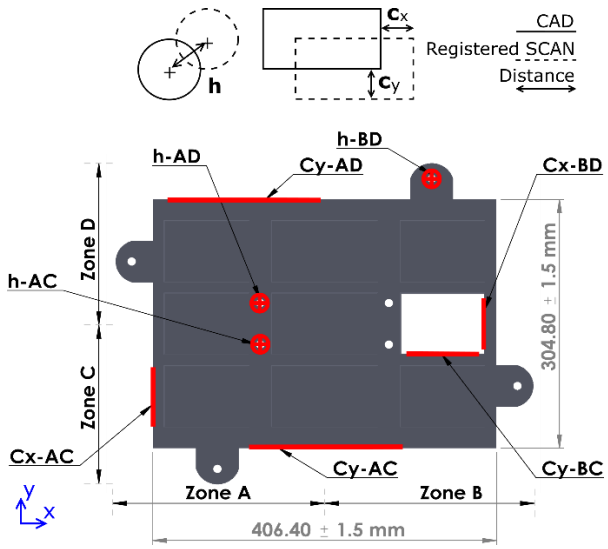

Table 5 – Case E1, Defect amplitude (manual measurement)

Defects (**in µm**)		Zone AC	Zone AD	Zone BC	Zone BD
Hole (**h**)	actual	**0**	**0**	-	**0**
	BOFR1	106	107	-	116
	BOFR2	**84**	**72**	-	**81**
Contour (**Cx** / **Cy**)	actual	**0 / 0**	**- / 0**	**- / 0**	**0 / -**
	BOFR1	**98** / 67	- / **33**	- / **85**	**147** / -
	BOFR2	104 / **66**	- / 34	- / **85**	150 / -

Table 6 – Case E2, Defect amplitude (manual measurement)

Defects (**in µm**)		Zone AC	Zone AD	Zone BC	Zone BD
Hole (**h**)	actual	**0**	**0**	-	**0**
	BOFR1	101	182	-	86
	BOFR2	**93**	**23**	-	**40**
Contour (**Cx** / **Cy**)	actual	**0 / 0**	**- / 0**	**- / 0**	**0 / -**
	BOFR1	58 / 49	- / 56	- / 53	**49** / -
	BOFR2	**48** / **44**	- / **45**	- / **44**	50 / -

Figure 5 – Defects and analyzed dimensions of the E1/E2 case studies (best estimations are underlined and emboldened)

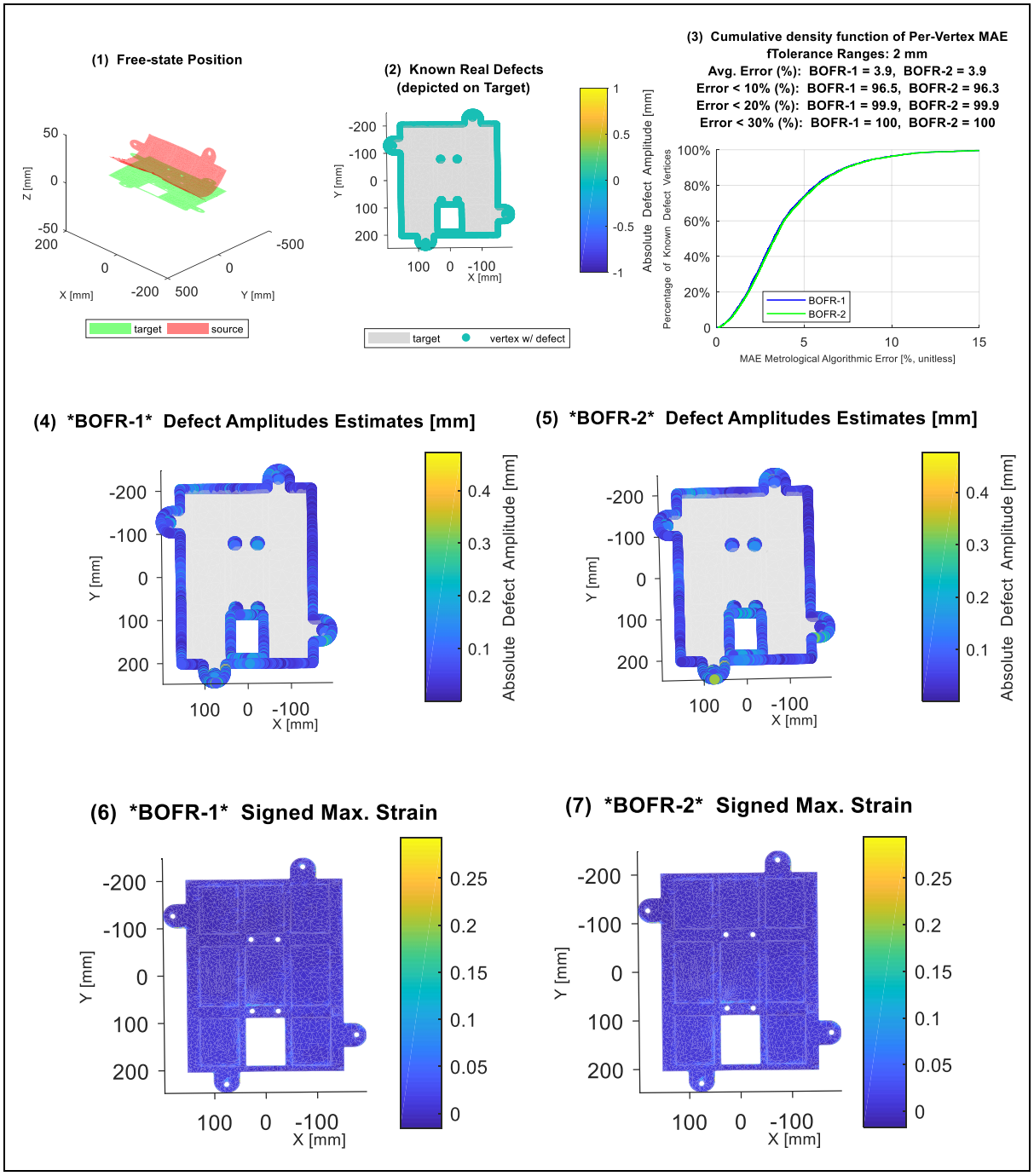

Figure 6 – Case E1

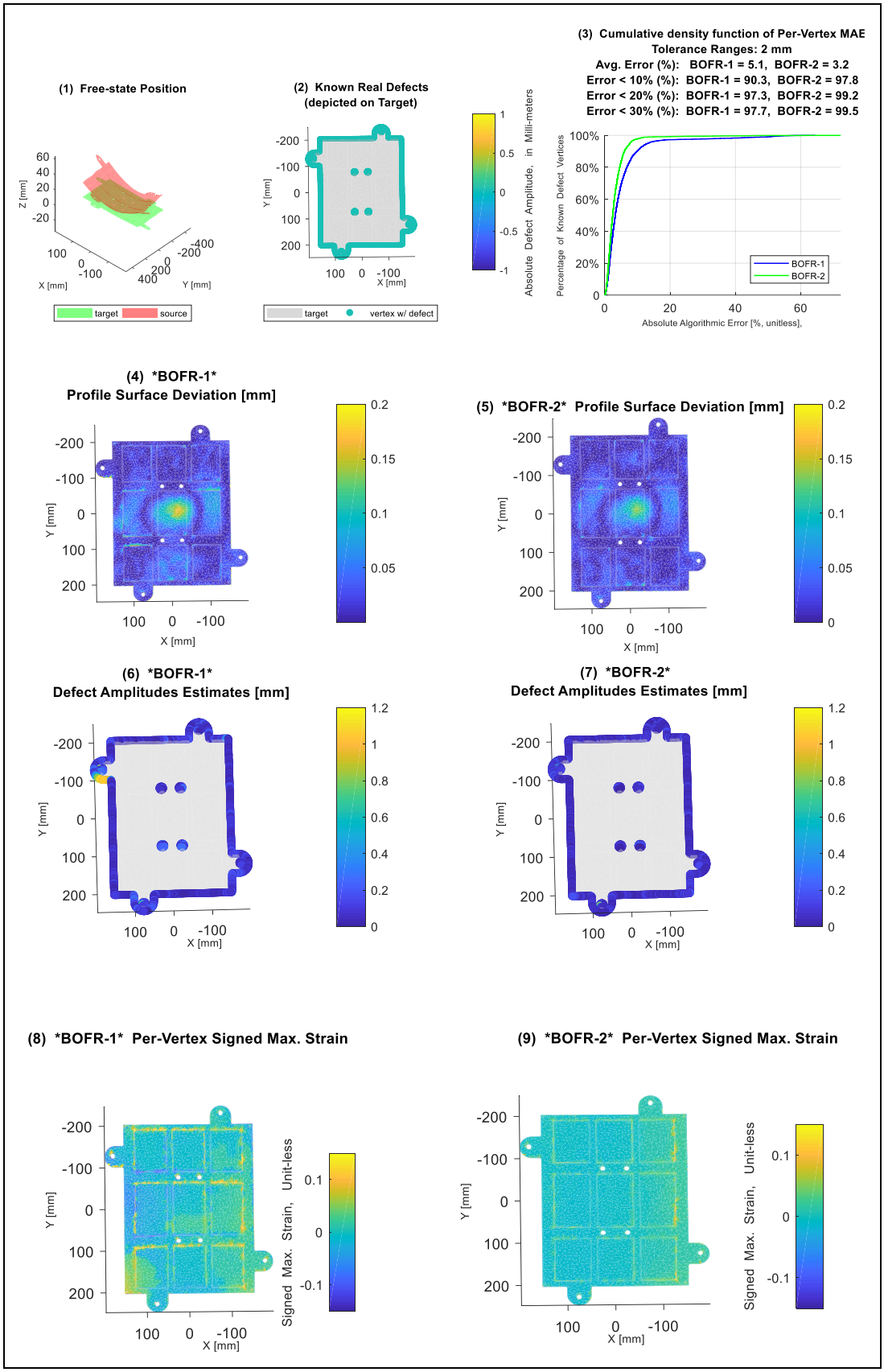

Figure 7 – Case E2

4 Discussion

The better results of BOFR-2 algorithm are explained firstly with the new formulation of the 2nd optimization objective (strain), and secondly with the new heuristic for picking the best member in the Pareto front (quality of superimposition):

	BOFR-1 [1]	BOFR-2
Step #4: 2nd optimization objective (1st objective = Hausdorff distance)	Stretch: Norm of local stretch values at mesh vertices, each of which being the **mean** of neighbor edges' elongation values (See Eq. 3).	Strain: Norm of local strain values at mesh vertices, each of which being the **maximum** of neighbor edges' elongation values. (See Eq. 5).
Step #5 "Optimality Heuristics" to pick the best member in the Pareto front	The solution featuring the smallest stretch criterion.	The solution featuring the best quality of superposition (QoS) (See Eq. 7).

Metrological algorithmic error: Figure 8 depicts all the metrological algorithmic errors emanating from the results. Lower algorithmic errors in the BOFR-2 are largely due to a better superposition between the registered SCAN and CAD. Figure 8 shows that 10% worst vertices aligned in BOFR-2 feature an error > 0.52%, compared to 2.9% for BOFR-1 in case A1 (BOFR-2 divides last decile the error by 5.6). The MAE of the 10% worst vertices' is also divided by 3.9 in case A2, 2.3 in case A3, and 1.6 on case E2. The two methods give similar performances on other test cases. For comparison, with similar case studies (skins), using a virtual fixture and a FE-based transformation model embedded into a constrained optimization [23] and GNIF [11], the level of error was between 5% and up to 12.5%.

Statistical algorithmic error: Across all cases, the statistical algorithmic errors in automatic defect identification results obtained by the BOFR-1/2 are shows in Figure 9. Lower algorithmic errors are largely due to an improved superposition between the registered SCAN and CAD.

Runtime: Total actual algorithm runtimes from start to final convergence for the BOFR are listed in Table 7. Figure 10 shows that BOFR 1&2 and AFDA [15] runtimes are comparable . The table also presents the number of black box evaluations before convergence, as well as the total number of CPD nonrigid registrar iterations.

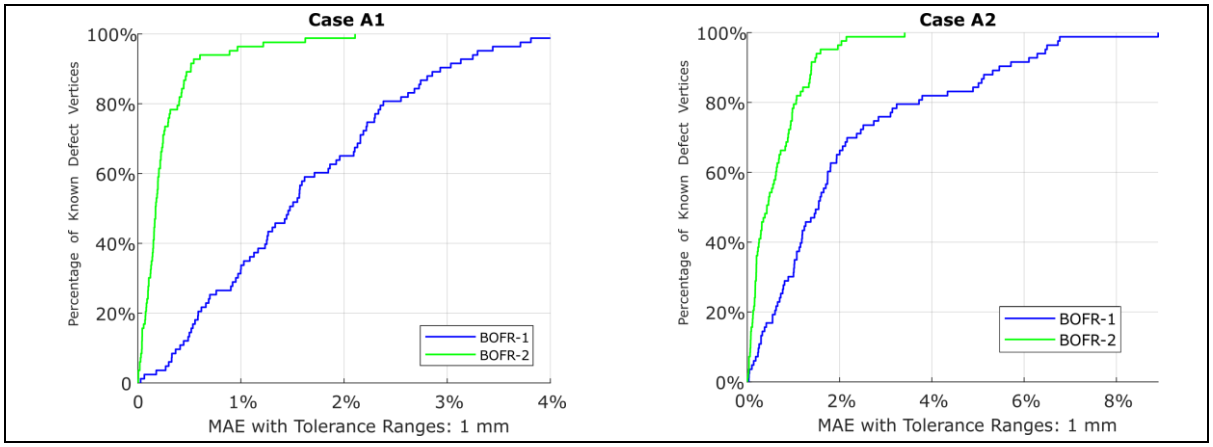

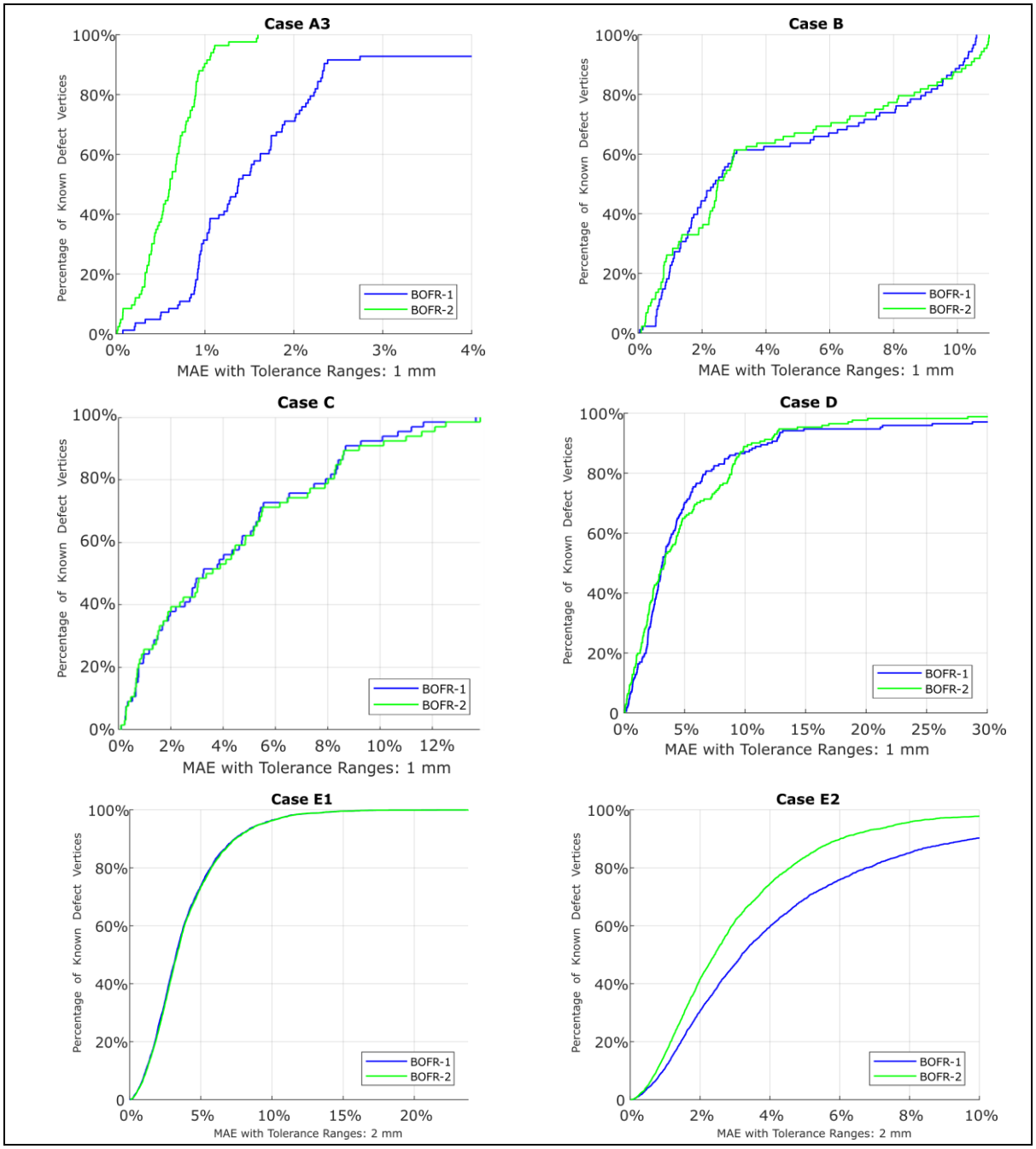

Figure 8 –Cumulative density function of per-vertex metrological algorithmic error [%] of BOFR-1 vs. BOFR-2, for KNOWN Defects (ALL Types) across all case studies (A1 to E2)

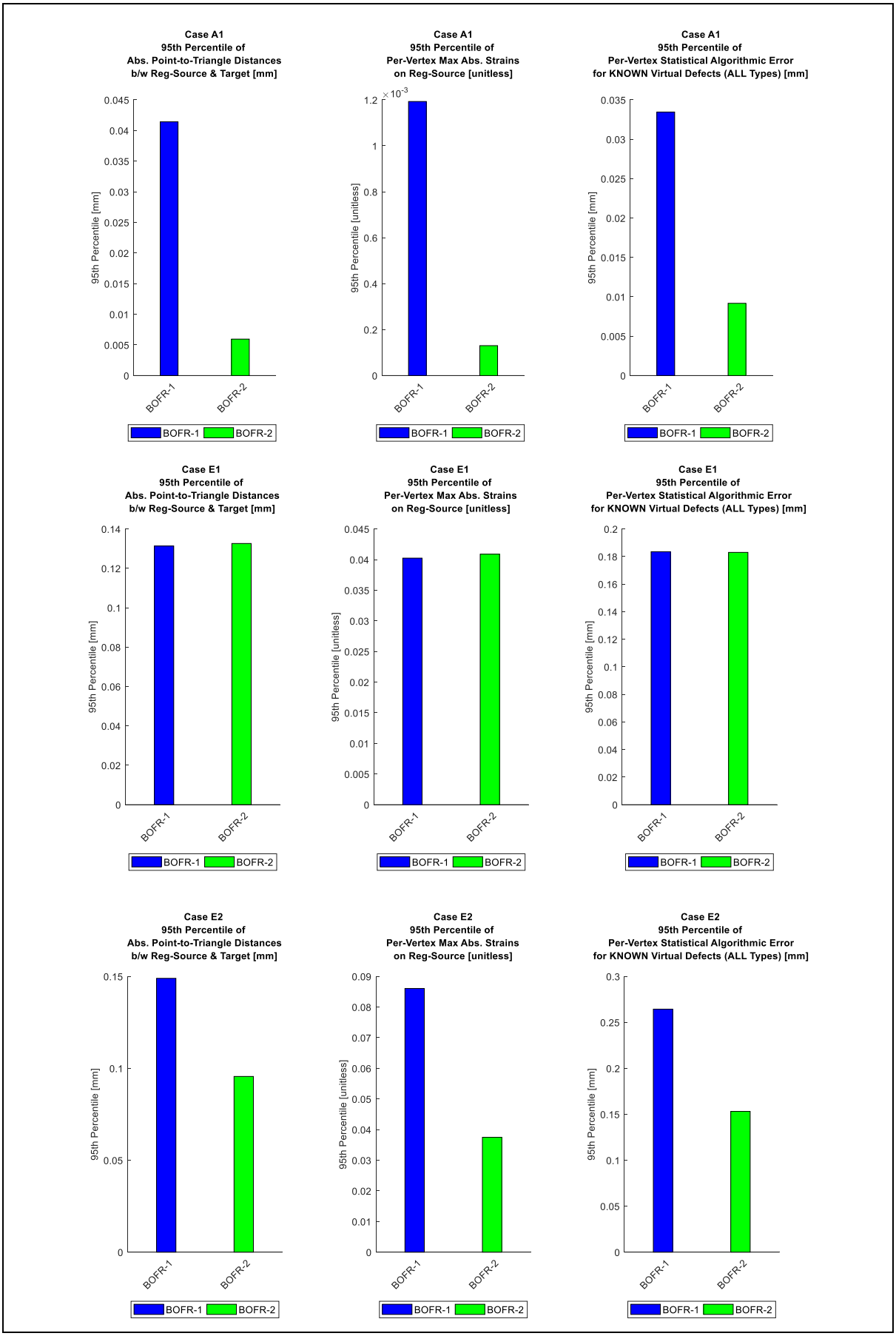

Figure 9 – Statistical quality comparison of BOFR-1 vs. BOFR-2 across all case studies (A1 to E2)

Table 7 – Runtimes of all case studies (A1 to E2) for BOFR-1 ; BOFR-2 ; AFDA methods

Case Study		# of Vertices	# of Triangles	Density [vertices per cm^2]	Runtime [seconds]			# of CPD Iterations			# of Black box Evaluations	
					ACPD	BOFR-1	BOFR-2	ACPD	BOFR-1	BOFR-2	ACPD	BOFR-1/2
A1	SCAN CAD	4010 1131	6952 1741	2.40 0.67	**604**	806	1026	3666	1606	**1535**	130	**50**
A2	SCAN CAD	4010 1131	6952 1741	2.40 0.67	**417**	591	518	2559	1567	**1405**	98	**50**
A3	SCAN CAD	4010 1131	6952 1741	2.40 0.67	651	598	**550**	4116	1751	**1646**	163	**50**
B	SCAN CAD	4019 1130	6956 1733	2.46 0.69	779	949	**736**	4631	**1322**	1368	179	**50**
C	SCAN CAD	3858 1069	6796 1697	0.55 0.15	**349**	642	644	3294	**1184**	1345	84	**50**
D	SCAN CAD	11053 2882	21156 5295	1.19 0.31	**2116**	2509	2616	4674	**1897**	1938	133	**50**
E1	SCAN CAD	6613 4112	9999 5000	5.34 3.32	2069	1734	**1454**	6533	3866	**3000**	109	**50**
E2	SCAN CAD	6468 3932	9999 5000	4.92 2.98	1535	**1045**	1270	5411	**2260**	3000	54	**50**

* Lowest values are underlined and emboldened

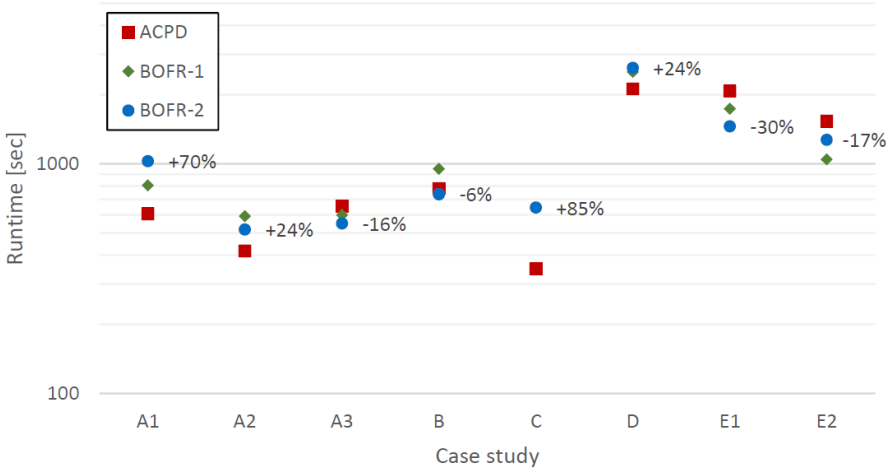

Figure 10 – Runtime comparison of BOFR-1 ; BOFR-2 ; AFDA across all case studies (A1 to E2). Labels are the percentage of supplementary BOFR-2 runtime of compared to ACPD runtime

5 Conclusion

A new methodology was proposed for the fixtureless inspection of compliant parts. The new approach, named BOFR-2, was developed to identify contour profile and hole center localization errors. This method consists of an optimization of the Coherent Point Drift (CPD) registration regularization parameters (lambda and beta) by using the Bi-Mads bi-objective method, which is independent of pre-defined internal weight parameters.

The BOFR-2 method was tested and validated on both virtual (simulated) and experimental (real) industrial case studies. A comparison with existing methods such as ACPD and BOFR-1 demonstrated more accurate results in the identification of the profile and localization defects.

The better quality of the registration with BOFR-2 algorithm compared to the first version BOFR-1[1] was measured with two metrics:

- Quality of superimposition (QoS): the registered mesh is closer to the target mesh (CAD), not only along the surface's normal direction, but also along the surface's tangent direction on the free edges located on the surface's boundary,
- Accuracy of error detection (MAE): the errors found on the registered mesh are closer to the real value of manually created defects.

The superiority of the BOFR-2 algorithm is explained with:

- the replacement of the stress criterion (norm of mean elongation values around each vertex) with BOFR-2's strain criterion (norm of maximal elongation values around each vertex), representing better the structural strain.
- the quality of superimposition (rate of vertices outside a tolerance envelope around the CAD mesh) that replaced the stretch heuristic to select the best solution in Pareto front.

Future works will involve (1) using a multi-objective method based on the Bi-Mads method [40] to include other criteria such as the minimization of the remanufacturing surface, (2) an extension to more complex geometries with non-uniform stiffness, such as bent plates, stiffeners, ribs, variable thicknesses, and (3) improving the robustness when the measurement noise amplitude changes with temperature variations during the data acquisition process.

Overall, the method in the present study could efficiently manage compliant parts at a lower cost, thus providing a competitive manufacturing advantage.

Acknowledgments

The authors would like to thank the *French Ministry of National Education, Higher Education, and Research (MENESR)*, the *Région Auvergne-Rhone-Alpes (*via *COOPERA Project GEOFLEX)*, and *École de technologie supérieure (ÉTS)* for their financial contribution. The *Laboratoire d'ingénierie des produits, procédés et systèmes (LIPPS)* associated with *ÉTS* provided CAD files for case studies A-B-C, and the real parts for case studies E1-E2.

Bibliography

[1] K. Babanezhad, G. Foucault, A. Tahan, et J. Bigeon, « BOFR-1: A Bi-Criterion Flexible Registration Method for Fixtureless Inspection of Compliant Parts », *Procedia CIRP Journal*, vol. 46, p. 307–310, 2016.

[2] G. N. Abenhaim, A. Desrochers, et A. Tahan, « Nonrigid parts' specification and inspection methods: Notions, challenges, and recent advancements », *International Journal of Advanced Manufacturing Technology*, vol. 63, n° 5–8, p. 741–752, 2012.

[3] A. Aidibe et A. Tahan, « IDB-CTB: Inspection of deformable bodies using curvature estimation and Thompson-Biweight test », *International Journal of Advanced Manufacturing Technology*, p. 1–15, 2014.

[4] A. Weckenmann et J. Weickmann, « Optical inspection of formed sheet metal parts applying fringe projection systems and virtual fixation », *Metrology and Measurement Systems*, vol. 13, n° 4, p. 321–334, 2006.

[5] A. Weckenmann, J. Weickmann, et N. Petrovic, « Shortening of Inspection Processes by Virtual Reverse Deformation », in *4th International Conference and Exhibition on Design and Production of Machines and Dies/Molds*, 2007, p. 21–23.
[6] C. Lartigue, F. Thiebaut, P. Bourdet, et N. Anwer, « Dimensional Metrology of Flexible Parts, Identification of Geometrical Deviations from Optical Measurements », in *Advanced Mathematical and Computational Tools in Metrology VII*, 2006, p. 196–203.
[7] A. Jaramillo, P. Boulanger, et F. Prieto, « Online 3D Inspection of Deformable Parts Using FEM Trained Radial Basis Functions », in *IEEE ICCV Workshops ICCV Workshops*, 2009, p. 1733–1739.
[8] R. Ascione et W. Polini, « Measurement of nonrigid freeform surfaces by coordinate measuring machine », *International Journal of Advanced Manufacturing Technology*, vol. 51, n° 9–12, p. 1055– 1067, 2010.
[9] A. Jaramillo, F. Prieto, et P. Boulanger, « Fast dimensional inspection of deformable parts from partial views », *Computers in Industry*, vol. 64, n° 9, p. 1076–1081, 2013.
[10] A. Jaramillo, F. Prieto, et P. Boulanger, « Fixtureless inspection of deformable parts using partial captures », *International Journal of Precision Engineering and Manufacturing*, vol. 14, n° 1, p. 77–83, 2013.
[11] H. Radvar-Esfahlan et A. Tahan, « RGNIF: Robust Generalized Numerical Inspection Fixture for the Metrology of Compliant Mechanical Parts », *The International Journal of Advanced Manufacturing Technology*, vol. 70, n° 5–8, p. 1101–1112, 2014.
[12] V. Sabri, S. A. Tahan, X. T. Pham, D. Moreau, et S. Galibois, « Fixtureless profile inspection of non-rigid parts using the numerical inspection fixture with improved definition of displacement boundary conditions », *The International Journal of Advanced Manufacturing Technology*, vol. 82, n° 5, p. 1343-1352, févr. 2016, doi: 10.1007/s00170-015-7425-3.
[13] V. Sabri, S. Sattarpanah, S. A. Tahan, J. C. Cuillière, V. François, et X. T. Pham, « A robust and automated FE-based method for fixtureless dimensional metrology of non-rigid parts using an improved numerical inspection fixture », *The International Journal of Advanced Manufacturing Technology*, vol. 92, n° 5-8, p. 2411-2423, 2017.
[14] F. Thiebaut, C. Lacroix, L. Andolfatto, et C. Lartigue, « Evaluation of the shape deviation of non rigid parts from optical measurements », *International Journal of Advanced Manufacturing Technology*, vol. 88, n° 5–8, p. 1937–1944, 2016.
[15] A. Aidibe et A. Tahan, « IDB-ACPD: Adapting the coherent point drift algorithm to the fixtureless dimensional inspection of compliant parts », *The International Journal of Advanced Manufacturing Technology*, 2015.
[16] A. Aidibe, A. Tahan, et G. N. Abenhaim, « Distinguishing profile deviations from a part's deformation using the maximum normed residual test », *WSEAS Transactions on Applied and Theoretical Mechanics*, vol. 7, n° 1, p. 18–28, 2012.
[17] M. Mounaud, F. Thiebaut, P. Bourdet, H. Falgarone, et N. Chevassus, « Assembly sequence influence on geometric deviations propagation of compliant parts », *International Journal of Production Research*, vol. 49, n° 4, p. 1021–1043, 2011.
[18] I. Gentilini et K. Shimada, « Predicting and evaluating the post-assembly shape of thin-walled components via 3D laser digitization and FEA simulation of the assembly process », *CAD Computer Aided Design*, vol. 43, n° 3, p. 316–328, 2011.
[19] G. N. Abenhaim, A. Tahan, A. Desrochers, et R. Maranzana, « IDI: A Novel Approach for the Inspection of Flexible Parts Without the Use of Special Fixtures », *Journal of Manufacturing Science and Engineering*, vol. 133, n° 1, p. 11009, 2011.
[20] B. Amberg, S. Romdhani, et T. Vetter, « Optimal step nonrigid ICP algorithms for surface registration », in *Proceedings of the IEEE Computer Society Conference on Computer Vision and Pattern Recognition*, 2007, p. 0–7,.
[21] A. Myronenko et X. Song, « CPD: Point Set Registration, Coherent Point Drift », *IEEE Transactions on Pattern Analysis and Machine Intelligence*, vol. 32, n° 12, p. 2262–2275, 2009.

[22] M. Haj Ibrahim, A. Aidibe, M. A. Mahjoub, A. Tahan, et B. Louhichi, « A novel approach to the inspection of deformable bodies by adapting the coherent point drift algorithm and using a clustering methodology », *The International Journal of Advanced Manufacturing Technology*, vol. 103, n° 1, p. 409-422, juill. 2019, doi: 10.1007/s00170-019-03554-z.
[23] G. N. Abenhaim, A. Desrochers, A. Tahan, et J. Bigeon, « A virtual fixture using a FE-based transformation model embedded into a constrained optimization for the dimensional inspection of nonrigid parts », *CAD Computer Aided Design*, vol. 62, p. 248–258, 2015.
[24] V. Sabri, S. Sattarpanah, J. C. Cuilliere, V. Francois, et A. Tahan, « Automatic fixtureless inspection of non-rigid parts based on filtering registration points », *The International Journal of Advanced Manufacturing Technology*, vol. 87, n° 1–4, p. 687–712, 2016.
[25] P. Franciosa, S. Gerbino, et S. Patalano, « A computer-aided tool to quickly analyse variabilities in flexible assemblies in different design scenarios », *International Journal of Product Development*, vol. 18, n° 2, p. 112-133, 2013.
[26] P. Franciosa, S. Gerbino, et D. Ceglarek, « Fixture capability optimisation for early-stage design of assembly system with compliant parts using nested polynomial chaos expansion », *Procedia CIRP*, vol. 41, p. 87-92, 2016.
[27] D. Gouyou, Y. Ledoux, D. Teissandier, et V. Delos, « Tolerance analysis of overconstrained and flexible assemblies by polytopes and finite element computations: application to a flange », *Research in Engineering Design*, vol. 29, n° 1, p. 55-66, janv. 2018, doi: 10.1007/s00163-017-0256-5.
[28] ISO 1101:2017, *Geometrical product specifications (GPS) — Geometrical tolerancing — Tolerances of form, orientation, location and run-out*. 2017.
[29] G. K. L. Tam *et al.*, « Registration of 3D Point Clouds and Meshes: A Survey from Rigid to Nonrigid », *IEEE Transactions on Visualization and Computer Graphics*, vol. 19, n° 7, p. 1199–1217, 2013.
[30] H. Chui et A. Rangarajan, « TPS-RPM: A new point matching algorithm for non-rigid registration », *Computer Vision and Image Understanding*, vol. 89, n° 2–3, p. 114–141, 2003.
[31] B. Jian et B. C. Vemuri, « TPS-L2: Robust point set registration using Gaussian mixture models », *IEEE Transactions on Pattern Analysis and Machine Intelligence*, vol. 33, n° 8, p. 1633–1645, 2011.
[32] Y. Gao, J. Ma, J. Zhao, J. Tian, et D. Zhang, « A robust and outlier-adaptive method for non-rigid point registration », *Pattern Analysis and Applications*, p. 1–10, 2013.
[33] Z. Zhou, J. Zheng, Y. Dai, Z. Zhou, et S. Chen, « Robust non-rigid point set registration using Student's-t mixture model », *PLoS ONE*, vol. 9, n° 3, 2014.
[34] A. P. Dempster, N. M. Laird, et D. B. Rubin, « Maximum likelihood from incomplete data via the EM algorithm », *Journal of the Royal Statistical Society Series B Methodological*, vol. 39, n° 1, p. 1–38, 1977.
[35] R. Sridharan, *Gaussian mixture models and the EM Algorithm (Lecture Notes - MIT CSAIL*. Cambridge, USA: MIT, 2017.
[36] L. Yuille et N. M. Grzywacz, « A Mathematical Analysis of the Motion Coherence Theory », *International Journal of Computer Vision*, vol. 3, n° 2, p. 155–175, 1989.
[37] L. M. Rios et N. V. Sahinidis, « Derivative-free optimization, A review of algorithms and comparison of software implementations », *Journal of Global Optimization*, vol. 56, n° 3, p. 1247–1293, 2013.
[38] C. Audet, G. Savard, et W. Zghal, « BiMADS: Multiobjective optimization through a series of single-objective formulations », *SIAM Journal on Optimization*, vol. 19, n° 1, p. 188–210, 2008.
[39] S. L. Digabel, « NOMAD: Nonlinear Optimization with the MADS Algorithm », *ACM Transactions On Mathematical Software*, vol. 37, n° 4, p. 1–44 15, 2011.
[40] B. Delaunay, *Sur la sphère vide (Delaunay Triangulation)," Bulletin de l'Académie des Sciences de l'URSS, Classe des sciences mathématiques et naturelles*. 1934.

[41] P. Cignoni, M. Callieri, M. Corsini, M. Dellepiane, F. Ganovelli, et G. Ranzuglia, « Meshlab: an open-source mesh processing tool. », in *Eurographics Italian chapter conference*, 2008, vol. 2008, p. 129-136.
[42] G. N. Abenhaim, A. Desrochers, et A. Tahan, « An investigation of the repeatability of nonrigid parts measurements, A case Study of an aluminum panel », in *Procedia CIRP*, vol. 10, 2013, p. 105–111.